Chinese Journal of Chemical Engineering 88 (2025) 335–347

Contents lists available at ScienceDirect

Chinese Journal of Chemical Engineering

journal homepage: www.elsevier.com/locate/CJChE

Full length article

Recycle of graphite and recovery of valuable metals from industrial-grade black mass of spent lithium-ion battery

Shang Liu [1, #], Kai Wang [1, #], Linlin Chen [1], Yaoguo Huang [1], Xianfu Sun [2], Qingyan Chu [1, *], Yali Zhang [1, *]

[1] School of Chemistry and Chemical Engineering, Shandong University of Technology, Zibo 255049, China
[2] Haidi Power Technology Co., Ltd., Zaozhuang 277400, China

ARTICLE INFO

Article history:
Received 10 March 2025
Received in revised form
18 April 2025
Accepted 28 May 2025
Available online 18 September 2025

Keywords:
Spent lithium-ion batteries
Graphite
Electrodeposition
Valuable metal recovery

ABSTRACT

The industrial-grade black mass of $LiFePO_4/LiNi_xMn_yO_4/C$ from spent lithium-ion battery is difficult to be recovered because of its complex composition. In this study, a recycling of graphite and comprehensive recovery of valuable metals from industrial-grade black mass of spent lithium-ion battery was proposed. Acid leaching can separate graphite and cathode materials well. The separated graphite was purified by roasting, and its electrochemical properties were tested. The specific discharge capacity of graphite purified at 600° are the best, which reach 342.46 $mA \cdot h \cdot g^{-1}$ at 0.1 C. After 50 cycles at 0.1 C, the capacity retention rate was 98.26%. The charge-discharge cycle stability was improved at high rates. Nearly 100% of copper can be recovered from leaching solution by electrodeposition. $FePO_4 \cdot 2H_2O$ is recovered by adjusting the pH of the solution to 2, and α-$FePO_4$ is obtained by roasting. Ni, Mn and Li can be recovered by precipitation separation. The optimum conditions for the recovery process was determined, and the mechanisms of the leaching and electrodeposition process were characterized by XRD, XPS, SEM-EDS.

1. Introduction

Lithium-ion batteries (LIBs), as an excellent electrical energy storage carrier with the advantages of higher cell voltage, higher energy density, long life, have been widely used in the fields of electronic products and electric vehicles [1]. With the continuous development of the lithium-ion battery industry, more and more lithium-ion batteries are facing the depletion of their service life leading to end-of-life. By 2030, the annual capacity of retired power batteries is estimated to be 100–120 GW·h globally [2], and spent LIBs contain a large amount of metals, such as lithium, nickel, manganese, and copper, which, if not handled appropriately, can cause serious pollution of the soil and groundwater, and will also become a resource of scrap metal. Therefore, from the point of view of resource recycling and environmental protection, the resource recycling of valuable metals from spent LIBs is of great significance to the economy and the environment [3].

Currently, the more mature recycling technologies for spent lithium-ion batteries are mainly divided into hydrometallurgy and pyrometallurgy, and pyrometallurgy mainly extracts and refines metals through high-temperature smelting and redox reactions [4,5]. Scholars have conducted a series of research, including chlorination roasting [6], sulfurization roasting [7,8], reduction roasting [9,10], *etc.* The main problem in pyrometallurgy is that lithium cannot be recovered effectively, and at the same time, the high energy consumption and the problem of generating exhaust gases are unavoidable. Different from pyrometallurgical technology, hydrometallurgy is achieved by placing cathode powder in a liquid phase system and transferring valuable metals as ions from the solid phase to the liquid phase through a series of chemical reactions. All kinds of valuable metals in the liquid phase are recovered, and the liquid-solid reaction cannot be carried out without the addition of inorganic acid or organic acid. Generally, the inorganic acids mainly include sulfuric acid solution [11], hydrochloric acid [12], nitric acid [13], phosphoric acid [14], *etc.*, and the organic acids mainly include citric acid [15], DL-malic acid [16],

* Corresponding authors.
E-mail addresses: chuqy@sdut.edu.cn (Q. Chu), zhangyali@sdut.edu.cn (Y. Zhang).
# These authors contributed equally to this work.

https://doi.org/10.1016/j.cjche.2025.05.046

ascorbic acid [17], tartaric acid [18], *etc*. Inorganic acids are more widely used due to the fact that inorganic acids exhibit stronger acidity and lower cost [19]. Since the crystal structure of the black mass of spent Li-ion batteries constructed by high-valence metals is difficult to destroy, the use of additives in the leaching process makes the solid–liquid leaching reaction proceed more thoroughly, and the most commonly used additive is hydrogen peroxide [20]. After the battery is disassembled, the aluminum foil and copper foil are separated, and the metal is mainly concentrated in the cathode active material [21], so the recycling work is mostly concentrated in the recovery of the metal in the cathode material. However, larger scale mechanical splitting was widely used in the lithium battery recycling process. Different types of cathode materials and graphite anodes are mixed, because its color is black, and called black mass of spent lithium-ion battery. Moreover, copper foils and aluminum foils are difficult to sieve completely during the separation process, which made the composition of black mass more complicated than cathode active materials. Therefore, recycling of valuable metals from black mass was a difficult challenge.

A process on the recycling of industrial-grade black mass of spent lithium-ion battery was investigated in this study. The main metals in the black mass was Li, Fe, Ni, Mn, Cu and a little of Al. H_2SO_4 and additive H_2O_2 were used to separate graphite and cathode materials, and the purified graphite is re-prepared into an anode. The main objectives are as follows: (1) to reveal the relationship between electrochemical properties of re-prepared graphite anode and purification temperature; (2) to study the recovery of copper by electrodeposition and explore its mechanism; (3) to synthesize iron phosphate directly in the solution and recover Li, Ni and Mn.

2. Experimental

2.1. Black mass and reagents

The black mass of spent Li-ion batteries (main components: $LiFePO_4$, $LiNi_xMn_yO_4$ and C) was provided by a battery recycling company of Shandong. Graphite electrode sheets (100 mm × 20 mm × 1 mm) used in the electrodeposition process were supplied by Inner Mongolia Wanxing Carbon Co. Ltd. and a dual DC regulated power supply (ATTEN APS3005S-3D) was used as the power source for electrodeposition. All chemicals (H_2SO_4, 30% (mass) H_2O_2, Na_2CO_3) were of analytical grade, and deionized water was used for all experimental procedures.

2.2. Recycle of graphite and re-preparation of anode

Because the cathode material in the black powder is soluble and the graphite is insoluble in acid, sulfuric acid solution is used as the leaching agent and H_2O_2 is used as the reducing agent to realize the separation of cathode material and anode graphite [22]. In order to remove the small amount of adhesive remaining in the graphite, the graphite was roasted in a tube furnace under N_2 atmosphere at 300, 450, and 600 °C for 30 min each. The roasted graphite is ground with a mortar to less than 0.0450 mm. The graphite, acetylene black and polyvinylidene fluoride (PVDF) at a mass ratio of 8:1:1 were dissolved homogeneously in *N*-methyl pyrrolidone (NMP) solution by using a homogenizer. And the mixed slurry was evenly coated on the surface of collector Cu foil and dried in a vacuum drying oven at 120 °C for 4 h. After drying, the anode is cut into a circular negative plate with a radius of 6 mm. CR2032 half-cell was assembled with the circular negative plate as anode, pure lithium as counter electrode, celgard-2400 as the separator, and 1 $mol \cdot L^{-1}$ $LiPF_6$ (ethylene carbide (EC): ethyl carbonate (DEC): ethyl methyl carboxylate (EMC) = 1:1:1, volume ratio) as the electrolyte specification.

2.3. The recovery of copper by electrodeposition in leach solution

Graphite sheets were used as electrode in electrodeposition process, and the output voltage was controlled by a dual DC regulated power supply. The effects of reaction voltage (1.5–3.5 V), electrode spacing (1.0–3.0 cm), electrodeposition time (2.0–4 h) and electrolyte concentration on the recovery efficiency of copper were investigated, and to the best experimental condition was determined.

2.4. The recovery of iron phosphate

Fe^{2+}, Fe^{3+}, and PO_4^{3-} existed in the solution, and $FePO_4$ would precipitate under certain conditions. Ferric ions in the leach solution after electrodeposition was used as the iron source and PO_4^{3-} was used as the phosphorus source. The initial pH of the leaching solution was about 0.5, sodium hydroxide solution was used to adjust the pH of the leaching solution after electrodeposition to 2. The slurry continued to be stirring for 2 h under air reflux, then aged at 90 °C for 2 h. After aging, the slurry was filtered, filtrate (1) was obtained, and the cake was dried at 60 °C for 6 h to obtain amorphous iron phosphate. The amorphous iron phosphate was roasted in a muffle furnace at 600 °C for 24 h to obtain α-quartz crystal iron phosphate. The effect of pH (1.5–3.5) on the precipitation process of iron phosphate was investigated.

2.5. The recovery of Li, Ni and Mn

The pH value of filtrate (1) was adjusted to 8 by adding sodium hydroxide solution to remove a small amount of Al and Fe, and filtered, the filtrate (2) was obtained. The pH of filtrate (2) was adjusted to 11, then filtered. The precipitate of manganese hydroxide containing nickel and filtrate (3) containing Li^+ was obtained. The filtrate (3) was concentrated at 90 °C. A certain amount of sodium carbonate was added and stirred for several minutes, and filtered immediately. The precipitate of Li_2CO_3 and filtrate (4) was obtained. The Li_2CO_3 was dried at 60 °C for 6 h. The filtrate (4) was evaporated to get the product of Na_2CO_3.

2.6. Characterization techniques

The elemental composition of black mass was measured by XRD and X-ray fluorescence analyses (XRF: ZSX Primus IV). The morphology and structure of the spent black mass, graphite, $FePO_4$ and Li_2CO_3 products were analyzed using a scanning electron microscope (SEM, Quanta 250, 3 kV of acceleration voltage), and the elemental distributions of black mass and graphite were measured using an energy spectrum analyses (EDS, 15 kV of the acceleration voltage and the SE2 secondary electronic detector as the detector). The electrochemical test of re-prepared graphite anode was performed at a voltage range of 0.01–2 V, using the NEWARE battery test system (CT-ZWJAS-T-1U). The cyclic voltammetry (CV) and electrolytic impedance spectroscopy (EIS) of the re-prepared graphite anode was tested by Chenhua Electrochemistry Workstation (CHI760E, B18441). The composition and structure of black mass, leaching residue, $FePO_4$, $Mn(OH)_2$ precipitate containing nickel, and Li_2CO_3 products was measured using an X-ray diffractometer (XRD, Bruker AXS D8 Advance, the sweep speed 2 $(^\circ) \cdot min^{-1}$, the tube voltage 40 kV, the current 40 mA) equipped with Cu-K_α; and the stability of $FePO_4 \cdot nH_2O$ was analyzed by a thermogravimetric analyses (TGA, SHIMADZU DTG-60H, 50 $ml \cdot min^{-1}$ of N_2/Air gas flow rate and 2 $^\circ C \cdot min^{-1}$ of the

Table 1
Main chemical components of the spent scrap.

Element	Li	Mn	Ni	Fe	Cu	Al
Composition/%	2.10	6.89	0.46	6.00	1.18	0.96
Element	C	O	F	P	Others	
Composition/%	40.04	32.50	5.88	3.12	0.87	

heating rate), and the number of crystalline water was determined.

3. Results and Discussion

3.1. Characterization of the black mass from spent lithium-ion battery

The content of each element in the black mass was shown in Table 1, and the distribution diagram was shown in Fig. 1(a). The XRD spectra was shown in Fig. 1(b), and it can be seen that the diffraction peaks of $LiFePO_4$, $LiNi_xMn_yO_4$ and C in the black mass were obviously presented. The TGA curves of the black mass were shown in Fig. 1(c), three stages of mass loss of the black mass can be observed. The first stage was below 200 °C, the mass was lost slowly, which was caused by the removal of moisture; the second stage was from 200 to 450 °C, the TG curve showed about 9% loss of mass, and such a loss was due to the pyrolysis of the organic binder and the organic solvents included; the third stage was after 450 °C, the TG curve showed a strong peak with a maximum loss of about 37%, which was due to the oxidation reaction of C in the black mass and the escape of the generated CO_2 gas [23] (see Tables 2 and 3).

The SEM and EDS images of the black mass were shown in Fig. 1 (d) and (e), respectively, from which the main substances of the black mass can be clearly observed. Combining with the distribution of Fe elements in the EDS image, we can see $LiFePO_4$ with a class-circular structure, as well as the flake graphite and $LiNi_xMn_yO_4$ with a spinel structure, which consisted of tetrahedral and octahedral small crystalline particles.

3.2. Recycle of graphite and electrochemical properties of the re-prepared anode

The graphite was separated from cathode material by acid leaching, and characterized by XRD, SEM and EDS. The results were presented in Fig. 2. The XRD spectrum (Fig. 2(a)) showed that the composition of leaching residue is C, and there was no other diffraction peak. Compared with Fig. 1(b), the diffraction peaks of $LiFePO_4$, $LiNi_xMn_yO_4$ disappeared, which proved that after the leaching process, $LiFePO_4$ and $LiNi_xMn_yO_4$ were well leached into the solution, and the leaching residue C was relatively pure. The SEM image (Fig. 2(b)) of the leaching residue showed that C in the leaching residue was flake graphite. The EDS surface-scan analysis (Fig. 2(d)) of the leaching residue showed that the elemental mapping of C was consistent with the structure of the flake. EDS spectrum (Fig. 2(c)) and elemental composition showed that the weight percentage of C is 97.30%, and the atomic percentage is 99.43%, which also indicated that the flake graphite after leaching was relatively pure. The thermogravimetric analysis (Fig. S1, Supplementary Material) on the graphite in an air atmosphere and found that the mass percentage content of the graphite was roughly consistent with the results obtained from energy-dispersive X-ray spectroscopy (EDS) testing.

As shown in Fig. 3(a), the XRD patterns of graphite purified at 300, 450, and 600 °C exhibit a dominant (0 0 2) peak at ~26.4°, confirming the preservation of the graphite structure. Notably, the peak intensity increases with higher temperatures, likely due to impurity removal (*e.g.*, binders). The layer spacing is calculated according to Bragg equation (Eq. (1)), and the result shows that the corresponding layer spacing is 0.3379, 0.3375, 0.3371 and 0.3366 nm, respectively. This is because that the carbon atoms of the graphite after high temperature purification migrate from the disordered structure to the ordered crystal structure, and the layer spacing decreases, which improves the degree of graphitization of the material [24]. The layer spacing has a direct effect on the properties of graphite such as conductivity, lithium ion diffusion rate and cycle stability. The smaller layer spacing can improve the conductivity of graphite and promote the speed of electron conduction, thus improving the discharge performance, charging speed of the battery, the cycle stability of graphite anode and prolonging the service life of battery.

The Barrett-Joyner-Halenda (BJH) method is used to evaluate the pore size and specific surface area of the recovered graphite material. Fig. 3(b)–(d) shows the nitrogen elution curve and pore size distribution of graphite and purified graphite at 300, 450°C and 600 °C. According to the classification method of IUPAC (International Union of Pure and Applied Chemistry), graphite and the purified graphite at 300 °C belong to the H3 hysteresis isotherm. According to the adsorption and desorption curve, it belongs to the H3 type flat slit structure, which is mainly composed of slit holes formed by the accumulation of flake particles, and tends to have no adsorption saturation at high relative pressure. It can be seen from the pore distribution that there is a wide void distribution between 10 and 50 nm, which is mainly a mesoporous structure. Fig. 3(d) shows that the graphite purified at 600 °C belongs to the H4 type and is also a narrow-slit hole. The pore size distribution shows a high peak value at 5 nm and a wide pore distribution at 10–50 nm. With the increase of graphitization degree, the proportion of micropores increases and the specific surface area is higher, which can provide more insertion sites for Li^+.

After grinding the graphite, the button cell was reassembled and its charge-discharge cycle performance was tested. Fig. S2 ((a) – (d)) shows the cyclic performance at small magnifications (0.1 C, 0.2 C, 0.5 C and 1 C). As can be seen from the figure, the specific discharge capacity of the anode reaches 283.15, 276.62, 270.34 and 230.18 $mA \cdot h \cdot g^{-1}$, respectively. The anode material prepared from unpurified graphite contains impurities that cause material volume changes, fatigue of the structure, and even fracture, resulting in poor stability during the charge-discharge cycle. After 50 cycles at 0.1 C rate, the capacity was 272.45 $mA \cdot h \cdot g^{-1}$, and the capacity of 96.22% was maintained. The coulomb efficiency is low in the first round, but reaches more than 99% after multiple cycles. During the first charging process, a solid electrolyte interface (SEI) film is formed, which is the key to protect the stability of the battery, and may also lead to some charge loss, thereby reducing the first coulomb efficiency [25]. It also shows good charge-discharge properties at magnifications of 2 C and 5 C.

The graphite contains a small amount of binder, which has a great impact on the battery capacity and cycle stability of the anode, so the recovered graphite is purified at different temperatures (300, 450, 600 °C). The cyclic properties after purification at 300, 450°C and 600 °C were shown in Figs. S2–S3 and Fig. 4. The specific electric capacity of the purified material at 300 °C can reach 313.65, 311.34, 302.45, 254.68 $mA \cdot h \cdot g^{-1}$ at 0.1 C, 0.2 C, 0.5 C, and 1 C (Fig. S3). Compared with unpurified graphite (Fig. S1), the capacity was greatly improved. After 50 cycles at 0.1 C, the capacity was 308.72 $mA \cdot h \cdot g^{-1}$, and the capacity retention rate was 98.43%. Roasting at 300° does not completely remove the binder, resulting in poor stability of the charge-discharge cycle. The specific

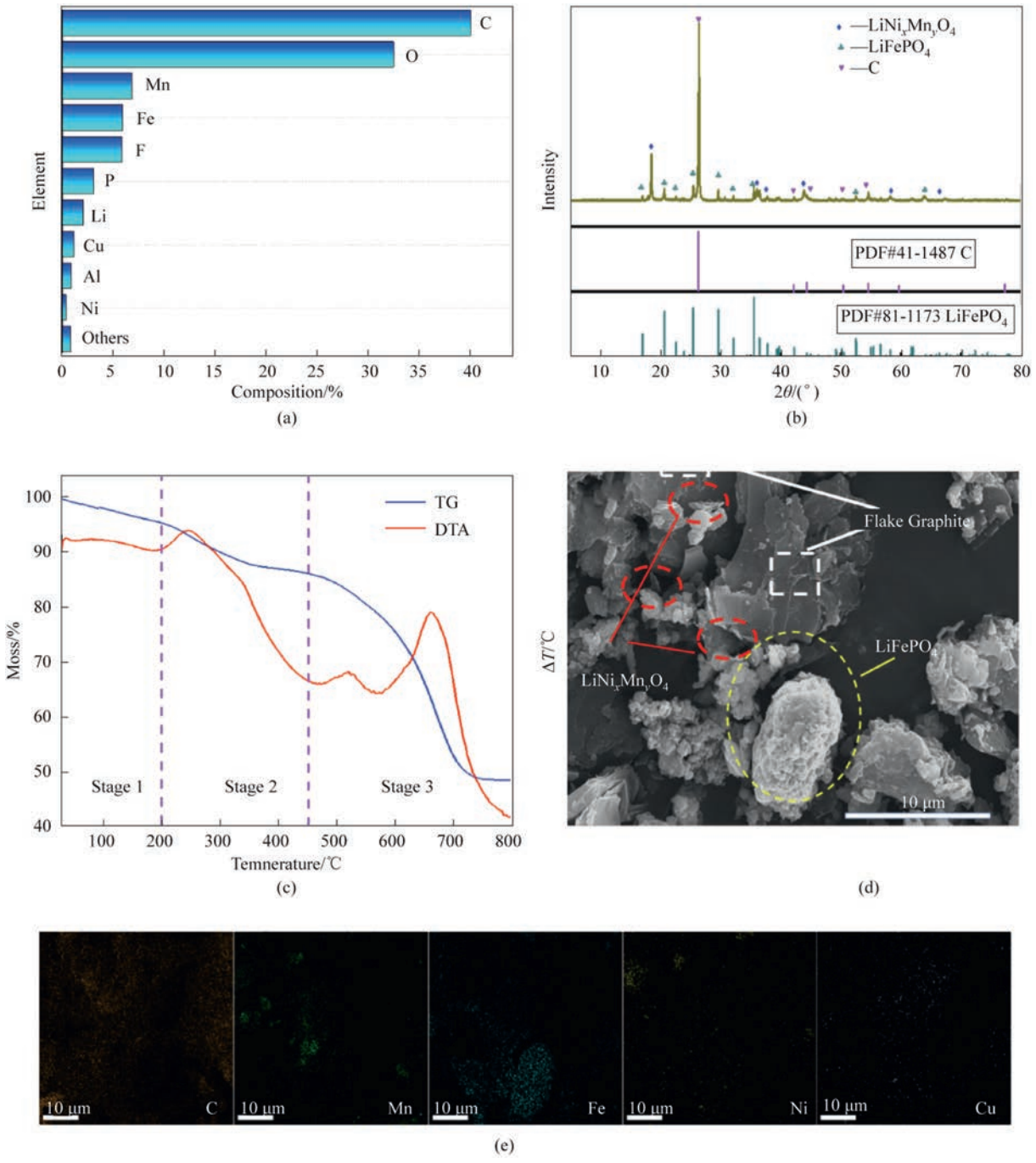

Fig. 1. Elemental content diagram (a); TGA curves (b); XRD spectra (c); SEM image (d); EDS image (e) of black mass spent lithium-ion battery.

capacity of the material purified at 450 °C can reach 341.65, 338.95, 312.57, 264.51 mA·h·g^{-1} at 0.1 C, 0.2 C, 0.5 C and 1 C (Fig. S4). Compared with the purified graphite at 300 °C, the capacity was improved. After 50 cycles at 0.1 C, the capacity was 327.31 mA·h·g^{-1}, the capacity retention rate was 95.80%, and the stability of the charge-discharge cycle was improved. The specific capacity of the purified material at 600 °C can reach 342.46, 336.81, 315.75 and 270.15 mA·h·g^{-1} at 0.1 C, 0.2 C, 0.5 C and 1 C (Fig. 4). After 50 cycles at 0.1 C, the capacity was 336.51 mA·h·g^{-1}, and the capacity retention rate was 98.26%. The charge-discharge cycle stability of the purified graphite anode at 600 °C was improved at high rates 2 C, 5 C(Fig. S5(e)–(f)). After high-temperature purification, the binder is removed and the degree of graphitization is increased, and the highly graphitized material has better structural stability and electrical conductivity, which

Table 2
Reduction potential of metal ions.

Reactions	$\phi = \phi^{\theta} + \frac{RT}{zF}\ln\frac{[O]}{[R]}$	ϕ/V
$Fe^{3+} + e^- = Fe^{2+}$	$0.771 - 0.025\ln[Fe^{2+}] + 0.025\ln[Fe^{3+}]$	0.701–0.841
$Cu^{2+} + 2e^- = Cu$	$0.337 + 0.012\ln[Cu^{2+}]$	0.287
$Ni^{2+} + 2e^- = Ni$	$-0.246 + 0.012\ln[Ni^{2+}]$	−0.266
$Mn^{3+} + e^- = Mn^{2+}$	$1.510 - 0.025\ln[Mn^{2+}] + 0.025\ln[Mn^{3+}]$	1.443–1.577

Table 3
Data on hydroxide precipitation.

Substance	C_1(M)	C_{min}(M)	pH_{start}(M)	pH_{end}(M)	K_{sp}
$Ni(OH)_2$	2.94×10^{-4}	1×10^{-5}	8.42	9.15	2.00×10^{-15}
$Mn(OH)_2$	3.01×10^{-3}	1×10^{-5}	8.91	10.15	2.00×10^{-13}
$Al(OH)_3$	6.10×10^{-4}	1×10^{-5}	4.11	4.71	1.3×10^{-33}
$Fe(OH)_3$	1.39×10^{-4}	1×10^{-5}	2.82	3.20	4×10^{-38}

can enhance the electrical conductivity and increase the charging and discharging efficiency of the battery. Materials with a high degree of graphitization have a more homogeneous pore structure and a larger specific surface area, which favors the diffusion and embedding of lithium ions inside the material and enables the storage of more lithium ions, improving the energy density and power performance of the cell. In short, after purification, the specific capacity increases at low magnification and changes little at 2 C and 5 C, but the stability is significantly improved.

CV cyclic voltammetry curve and EIS impedance test results are shown in Fig. S6 and Fig. 5. The CV curve shows the voltage response of the battery prepared with graphite as anode material under different charging and discharging states. The oxidation peak is about 1.0 V, the reduction peak is about 0.25 V, the CV curve shape and the characteristic peak position of the graphite roasted at different temperatures are similar, indicating that the electrochemical reaction of the materials is the same. Due to the different degree of graphitization of graphite at different temperatures, the shape and sharpness of the peak tip are slightly different due to the effect of electrochemical reaction rate and electrolyte diffusion. All the four samples have good electrochemical reversibility.

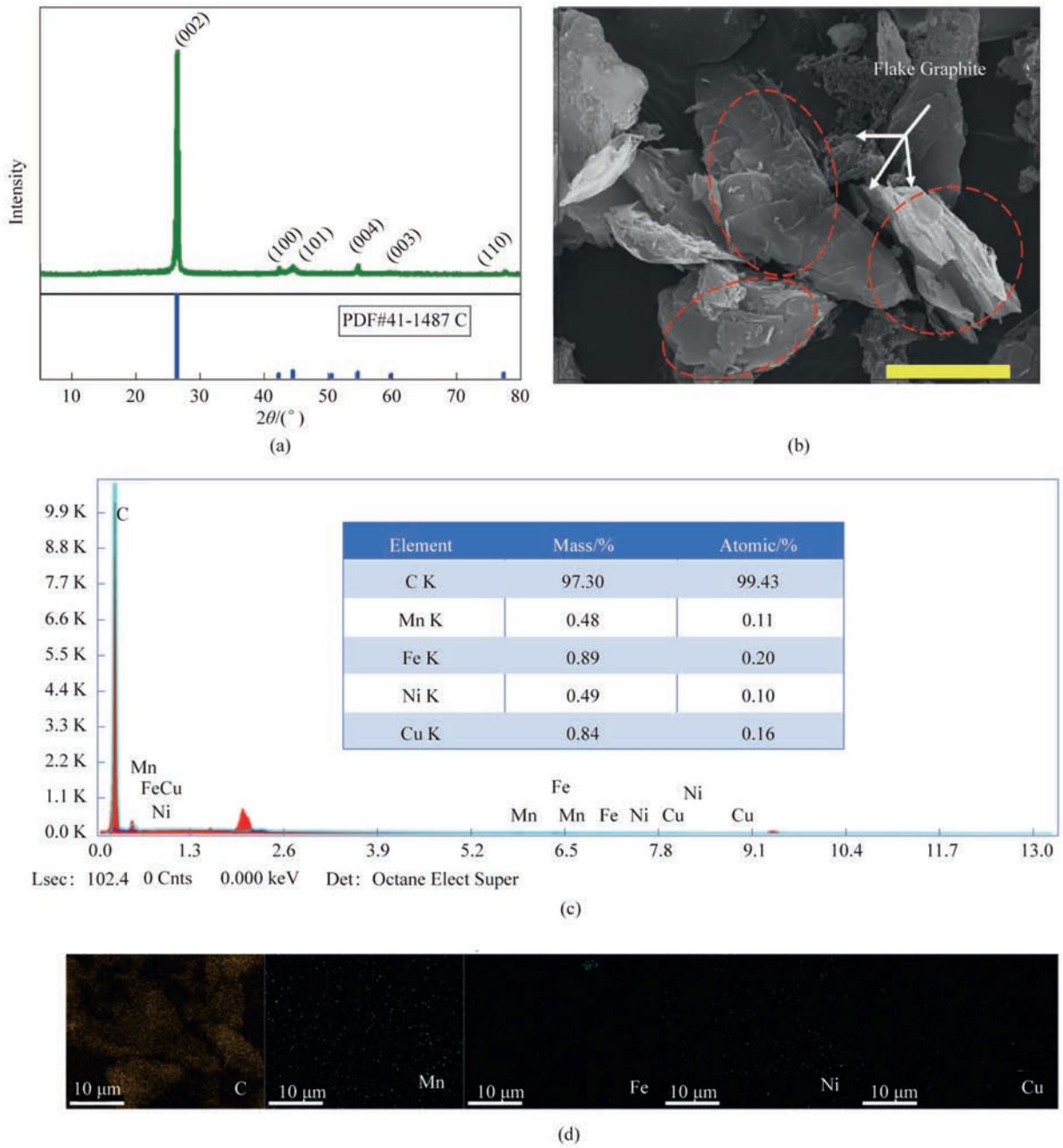

Element	Mass/%	Atomic/%
C K	97.30	99.43
Mn K	0.48	0.11
Fe K	0.89	0.20
Ni K	0.49	0.10
Cu K	0.84	0.16

Fig. 2. XRD spectrum (a); SEM image (b); EDS energy spectrum (c); and elemental mapping (d) for the graphite.

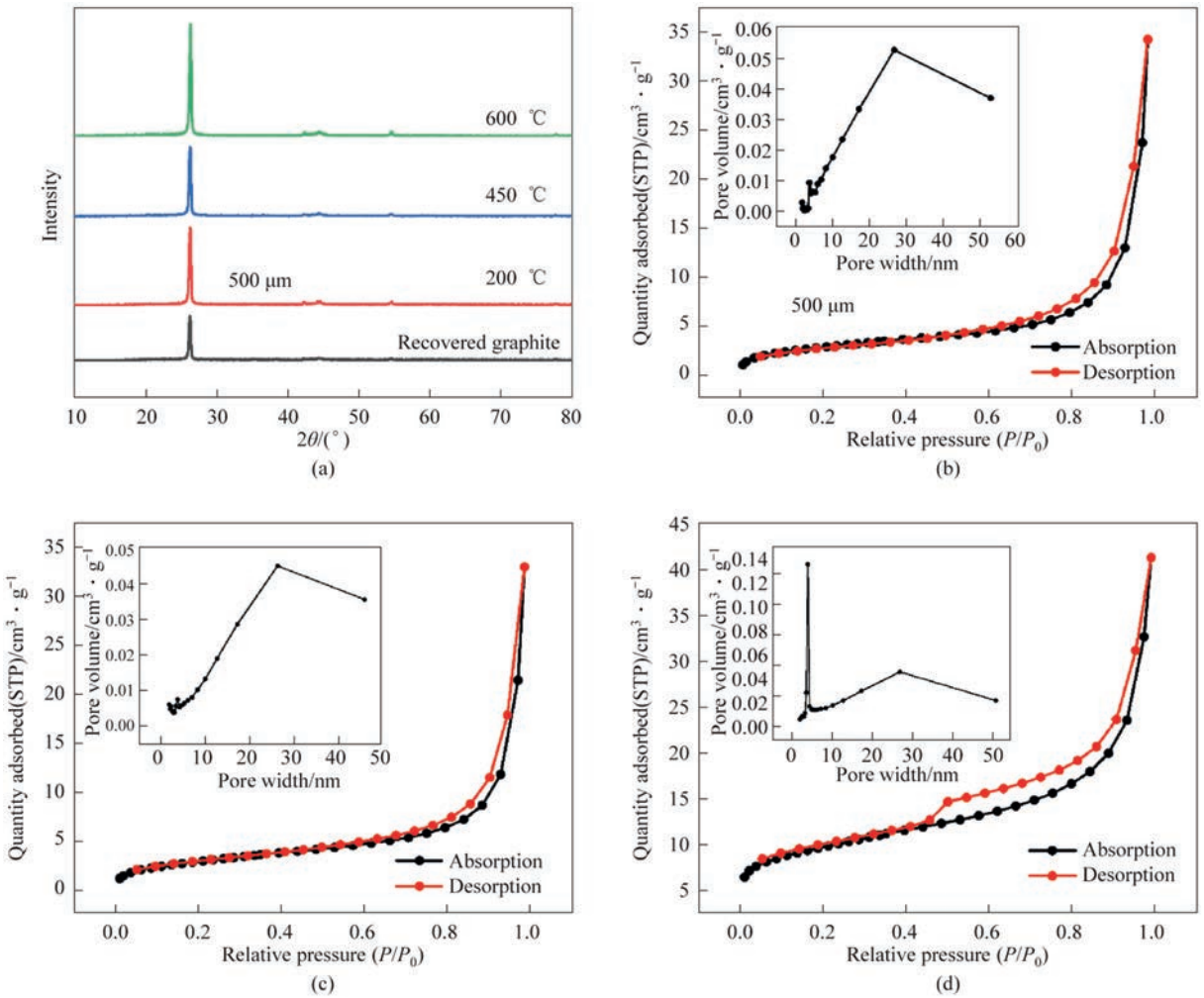

Fig. 3. XRD of graphite at different purification temperatures (a); nitrogen absorption and desorption curve of recovered graphite (b); nitrogen absorption and desorption curve of purified graphite at 300 °C (c); nitrogen adsorption and desorption curve of purified graphite at 600 °C (d).

3.3. Copper recovery by electrodeposition and mechanism analysis

In $LiFePO_4$ materials, Fe^{2+} is oxidized to Fe^{3+} under the action of oxidizing substances (H_2O_2, Ni^{3+}, Mn^{4+}), while in $LiNi_xMn_yO_4$ materials, Ni^{3+}, Mn^{4+} are reduced to Ni^{2+} and Mn^{2+} by reducing substances (H_2O_2, Fe^{2+}), The chemical equation is shown in Eq. (1). Under the action of sulfuric acid solution and H_2O_2, the copper foil doped in the black powder dissolves and transforms into Cu^{2+}.

$$LiNi_xMn_{1-x}O_2 + 6H^+ + H_2O_2 + LiFePO_4 \rightarrow xNi^{2+} + (1-x)Mn^{2+} + 2Li^+ + Fe^{3+} + PO_4{}^{3+} + 4H_2O \quad (1)$$

The variation of voltage during electrodeposition was directly related to the electrochemical reaction rate and energy consumption. The effects of voltage (1.5–3.5 V), electrode spacing and electrodeposition time on the copper recovery were experimentally investigated. The effect of voltage on the recovery efficiency was shown in Fig. 6(a), it could be seen that the recovery efficiency of Cu increased with increasing the voltage. When the voltage reached 3.5 V, the recovery efficiency of Cu reached 87.50%. The increase of voltage promoted the movement of electrons and increased the current density, which improved the efficiency of ion migration and electrodeposition efficiency, leading to an increase in the recovery efficiency. After the voltage increased to 3.5 V, the H^+ would gain electrons violently, and the increase in secondary reactions is detrimental to the deposition of copper and results in more electrical energy consumption.

The effect of electrode spacing (1.0–3.0 cm) on copper recovery was investigated at a voltage of 3.5 V and electrodeposition time of 2 h. The results were shown in Fig. 6(b) and showed that the recovery efficiency of Cu decreased with the increase of electrode spacing, and the recovery efficiency reached 94.28% at an electrode spacing of 1.0 cm. When the electrode spacing increased to 3.0 cm, the recovery efficiency of Cu decreased to 65.34%. With increasing electrode spacing, the ohmic loss due to electrolyte ionic resistance increased, which led to a decrease in the recovery efficiency. On the other hand, the larger electrode spacing, the higher the mass transfer resistance, the longer the diffusion path, and the longer the electrodeposition time.

The relationship between recovery efficiency and electrodeposition time was shown in Fig. 6(c), it could be seen that with the increase of time, the recovery efficiency of Cu increased, and reached 100% after 2.5 h. The recovery efficiency of Cu was improved with the increase of time. Fig. 6(d) showed the relationship between the concentration factor and the recovery efficiency under the experimental conditions: 3.5 V of voltage, 1.0 cm of electrode spacing, 3.0 h of electrodeposition time. It could be

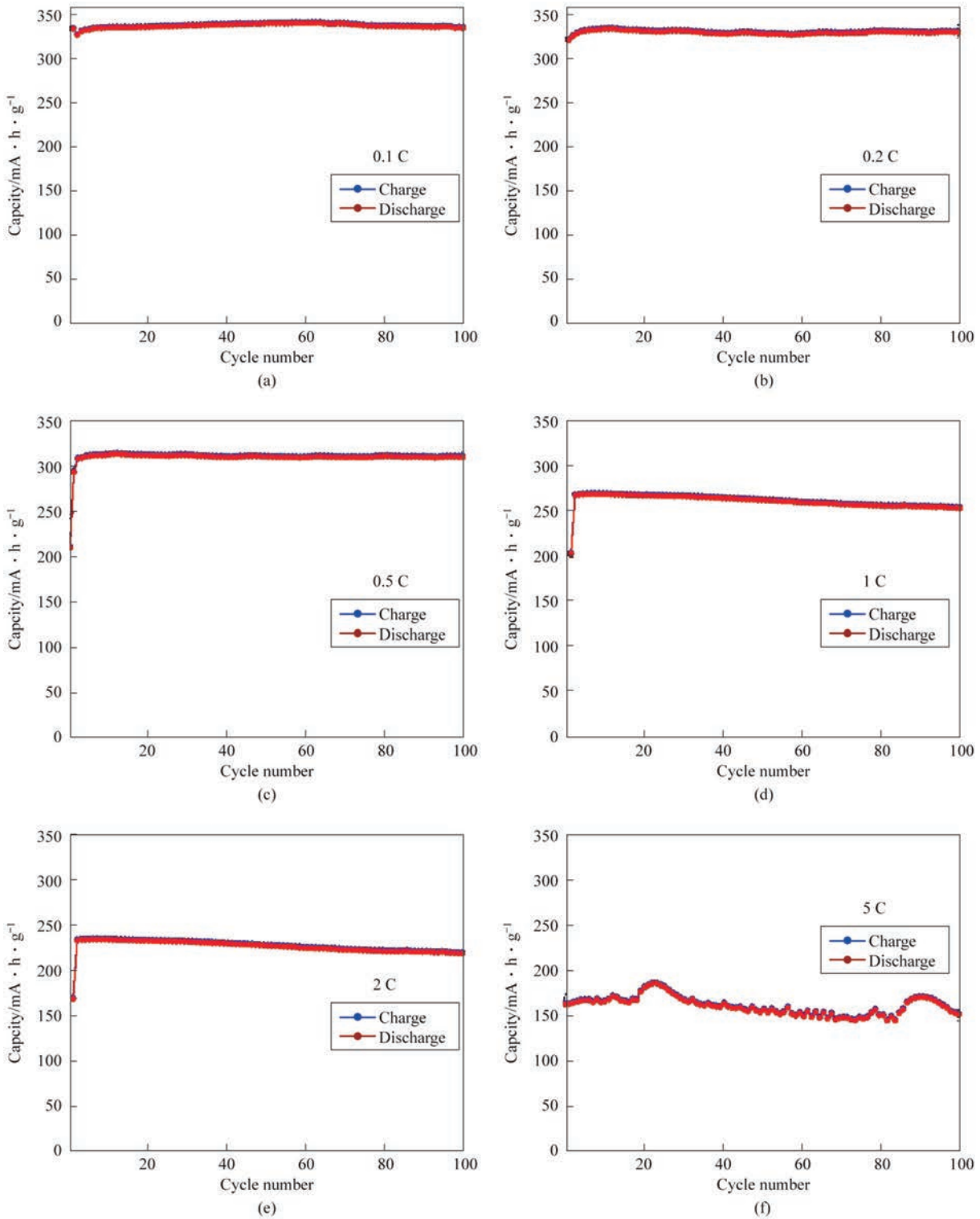

Fig. 4. The charge-discharge cycle performance of the anode material prepared from purified graphite at 600 °C.

seen that under the same experimental conditions, the recovery efficiency did not decrease proportionally with the increase of concentration multiples. The trend of the decreasing in Cu recovery efficiency gradually became slower, which was due to the fact that with the increase of concentration multiples, the concentration of ions in the solution increased, which in turn increased the conductivity of the solution and decreased the resistance of the solution.

Fig. 7 showed cathodic graphite sheet picture after electrodeposition and XRD spectrum of deposited copper, it could be observed that a layer of purplish-red material was deposited on the graphite sheet, which was formed by reduction of copper in

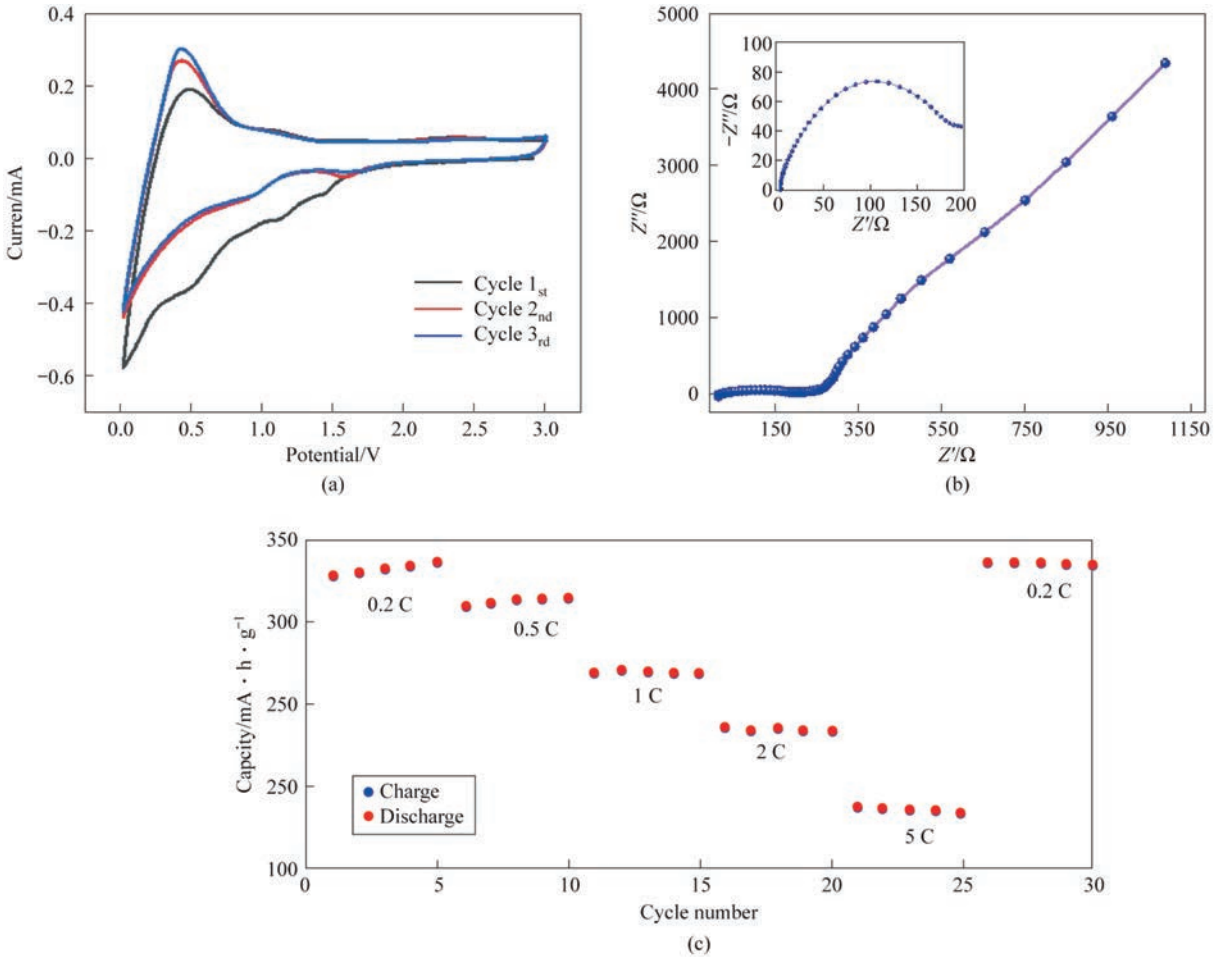

Fig. 5. CV(a), EIS (b) and magnification performance diagram (c) of the anode re-prepared by purified graphite at 600 °C.

the leaching solution in the cathodic deposition during electrodeposition process. XRD spectrum showed that the electrodeposited products were mainly monomeric Cu and Cu_2O, which was because of two microelectrochemical steps in the electrodeposition reduction process of Cu(II). Cu(II) would first be reduced to the Cu(I) valence state to form the product Cu_2O, and then Cu(I) would be reduced further to form Cu(0) as shown in reactions(Eqs. (2) and (3)).

$$2Cu^{2+} + H_2O + 2e^- = Cu_2O + 2H^+ \quad (2)$$

$$Cu_2O + 2e^- + 2H^+ = 2Cu + H_2O \quad (3)$$

Fig. 8 showed the mechanism of the electrodeposition process, the reduction reaction occurred at the cathode, the Cu^{2+} in the leaching solution migrated to the cathode under the action of an electric field, got electrons to be reduced to the low valence state (Cu_2O and Cu), and deposited on the surface of the graphite sheet. Mn^{3+}/Mn^{2+} and Fe^{3+}/Fe^{2+} electrode pairs had higher reduction potentials than those of Cu^{2+}/Cu, which were more helpful to gain electrons at the cathode for the reduction reaction, Mn^{3+} was reduced to Mn^{2+}, and Fe^{3+} was reduced to Fe^{2+}. However, since they were in ionic state, they did not affect the quality of copper. At the same time, Fe^{2+} was free in the electrolyte, so Fe^{2+} would lose electrons to be oxidized to Fe^{3+} at the anode, and Fe^{3+} would gain electrons to be reduced to Fe^{2+} at the cathode, so after the electrodeposition process, Fe^{2+} and Fe^{3+} existed in solution at the same time.

3.4. Recovery of $FePO_4$ and analysis of recovery products

When the iron ions in the leachate after electrodeposition are used as the iron source and PO_4^{3-} as the phosphorus source, and the pH is adjusted to 2, $FePO_4 \cdot nH_2O$ is generated. The picture of $FePO_4 \cdot nH_2O$ product and its XRD spectrum was shown in Fig. 9(a), the obtained $FePO_4 \cdot nH_2O$ is a white solid, in the spectrum there is a broad peak between 20° and 30°, which indicated that the product is poorly crystalline and the amorphous phase was dominant [26].

To determine the number of water molecules in $FePO_4 \cdot nH_2O$, thermogravimetric analyses of $FePO_4 \cdot nH_2O$ were conducted at a heating rate of 5 °C·min^{-1}. The TG-DTA curve of $FePO_4 \cdot nH_2O$ in air atmosphere was shown in Fig. 9(b). From the figure, it could be seen that apparent mass loss appeared in the range of 100–200 °C, and the heat absorption effect of DTA occurred mainly at 180 °C. The mass loss in the TG curve after stabilization was measured to be 22.01%, which is similar to the ideal value of $FePO_4$ binding two water molecules (19.28%), the excessive mass loss was probably due to water adsorption by the sample. The mass after dehydration was about 78%, corresponding to the formation of $FePO_4$ [27].

Fig. 9(c), (d) showed the SEM images of α-quartz crystalline $FePO_4$, it could be seen from the figure that the microscopic state of

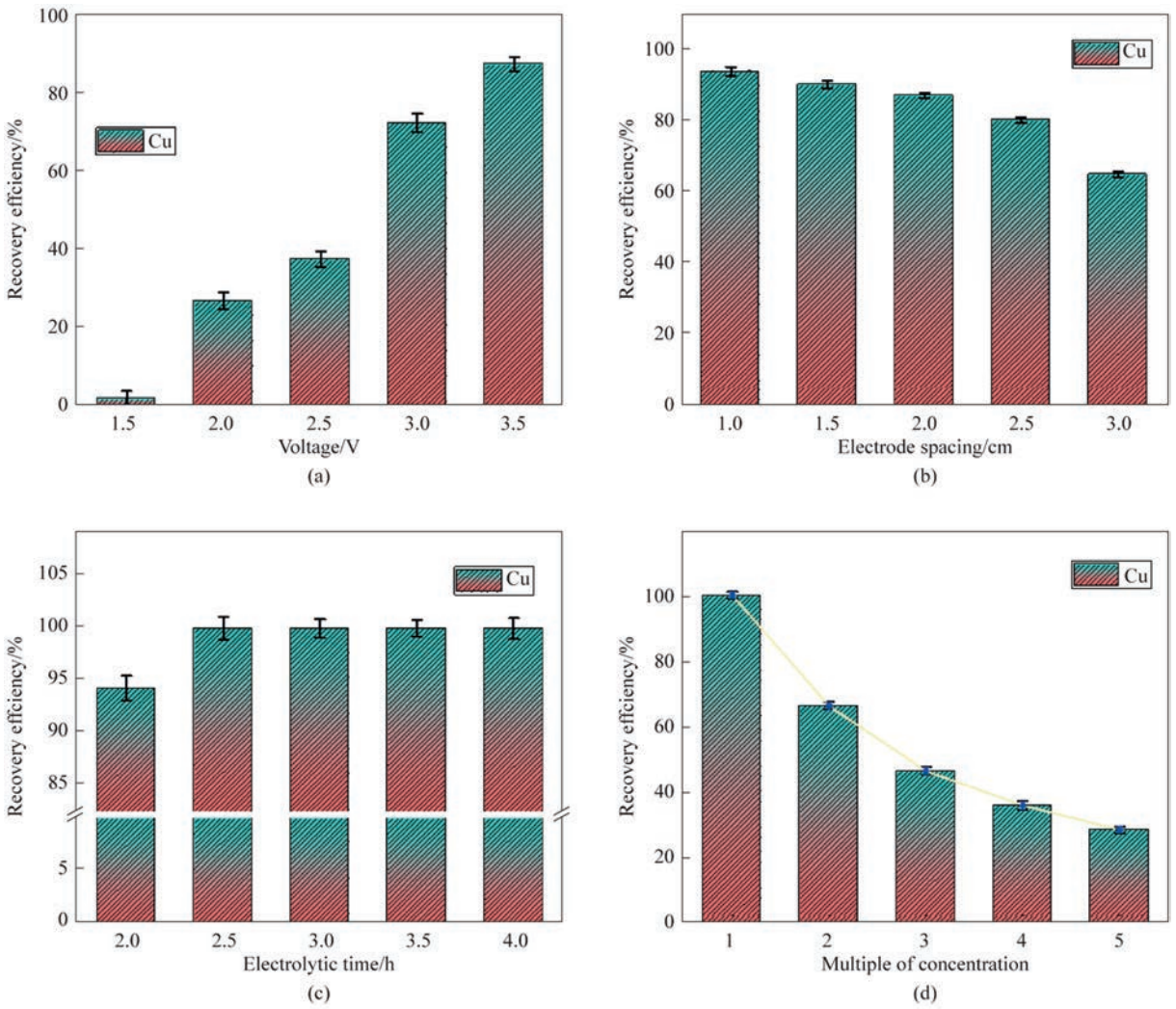

Fig. 6. Effect of voltage (a); electrode spacing (b); electrodeposition time (c); concentration factor (d) on Cu recovery efficiency.

$FePO_4$ is made of many fine particles, which was caused by crystal aggregation of amorphous $FePO_4 \cdot nH_2O$ during the roasting process at 600 °C. Fig. 9(e) showed the XRD spectrum of the recovered iron product by adjusting different pH values, it could be seen that the XRD spectrum of the product obtained at pH 1.5 and 2.0 matched with α-quartz $FePO_4$ (PDF#84-0876), which proved it was $FePO_4$. The XRD spectrum of the product obtained at pH 2.5, 3.0 and 3.5 showed $Na_3Fe_2(PO_4)_3$ and Fe_2O_3 diffraction peaks, and the characteristic peak of $FePO_4$ disappeared, which proved the kind of

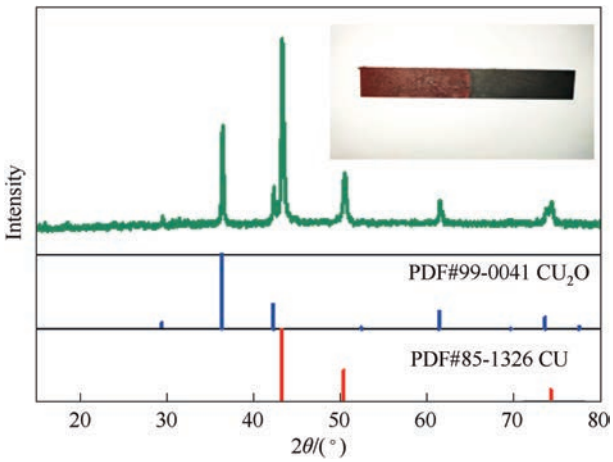

Fig. 7. Cathodic graphite sheet picture after electrodeposition and XRD spectrum of deposited copper.

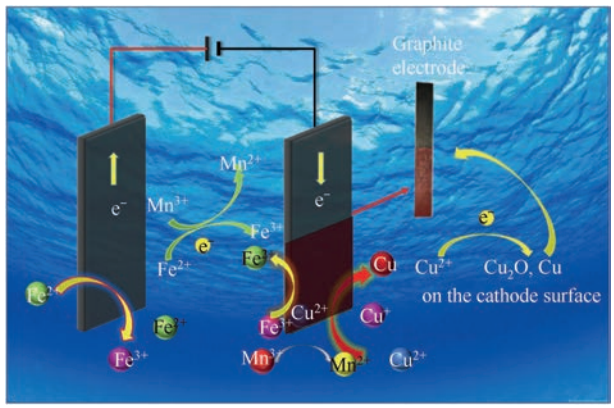

Fig. 8. Mechanism diagram of electrodeposition process.

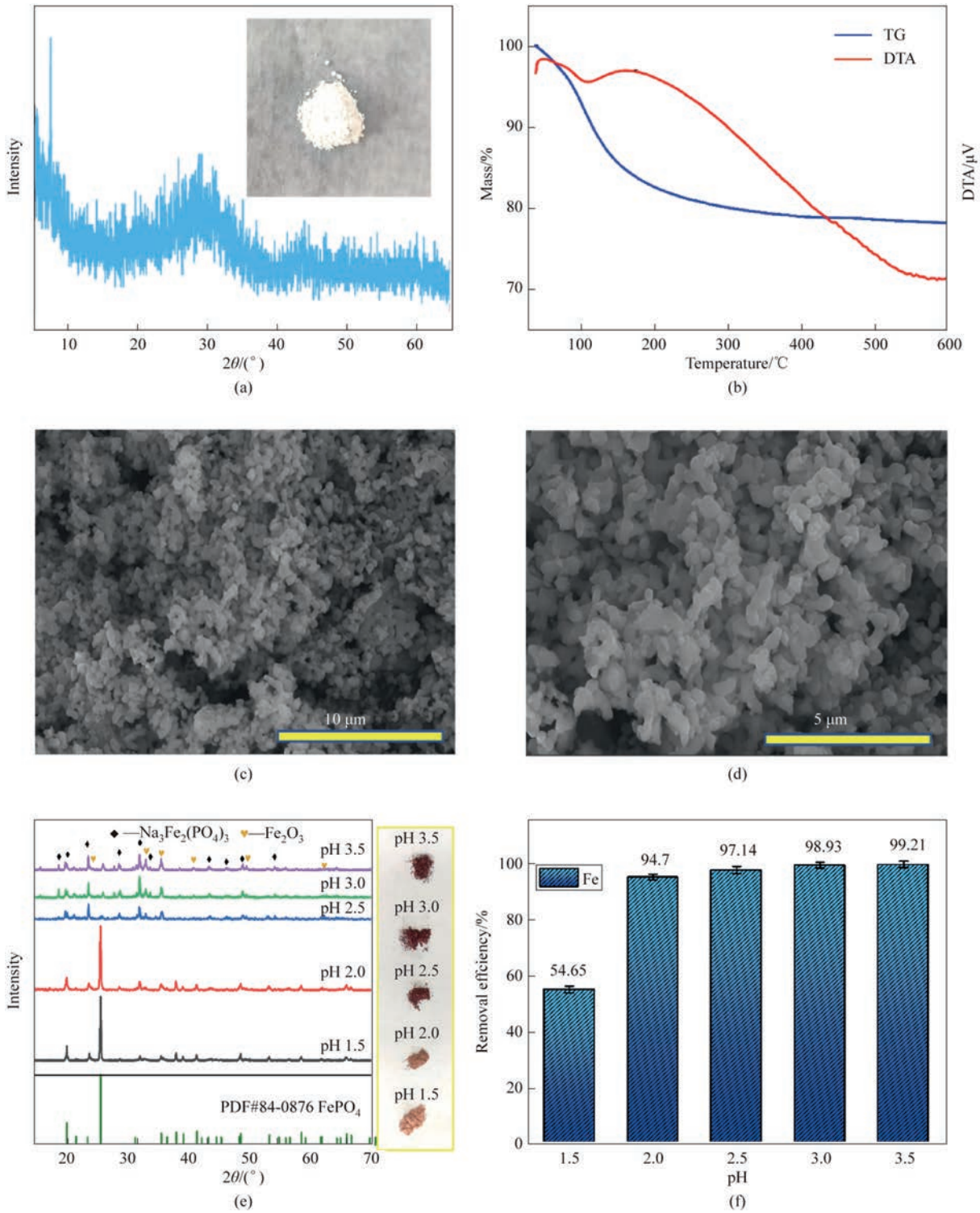

Fig. 9. XRD of amorphous $FePO_4 \cdot 2H_2O$ (a); TG-DTA of amorphous $FePO_4 \cdot 2H_2O$ (b); SEM images of $FePO_4$ (c-d); XRD of precipitate corresponding to Fe at different pH values (e); recovery efficiency of Fe at different pH values (f).

products changed. When pH value was is greater than 2.5, $Fe(OH)_3$ is precipitated in the solution, Fe_2O_3 was formed during roasting.

In addition, the color of the product at pH 1.5 and 2.0 was light pink, while after the pH exceeded 2.0, the color of the product changed to reddish brown, which corresponded to the color of Fe_2O_3. combined with Fig. 9(f) the recovery efficiency of iron under different pH conditions, with the increase of pH value Fe recovery efficiency increased, but due to the pH value over 2.0, precipitation product was no longer the target product $FePO_4$, so in adjusting the pH value of the recovery of $FePO_4$ process should be strictly control the pH value [28].

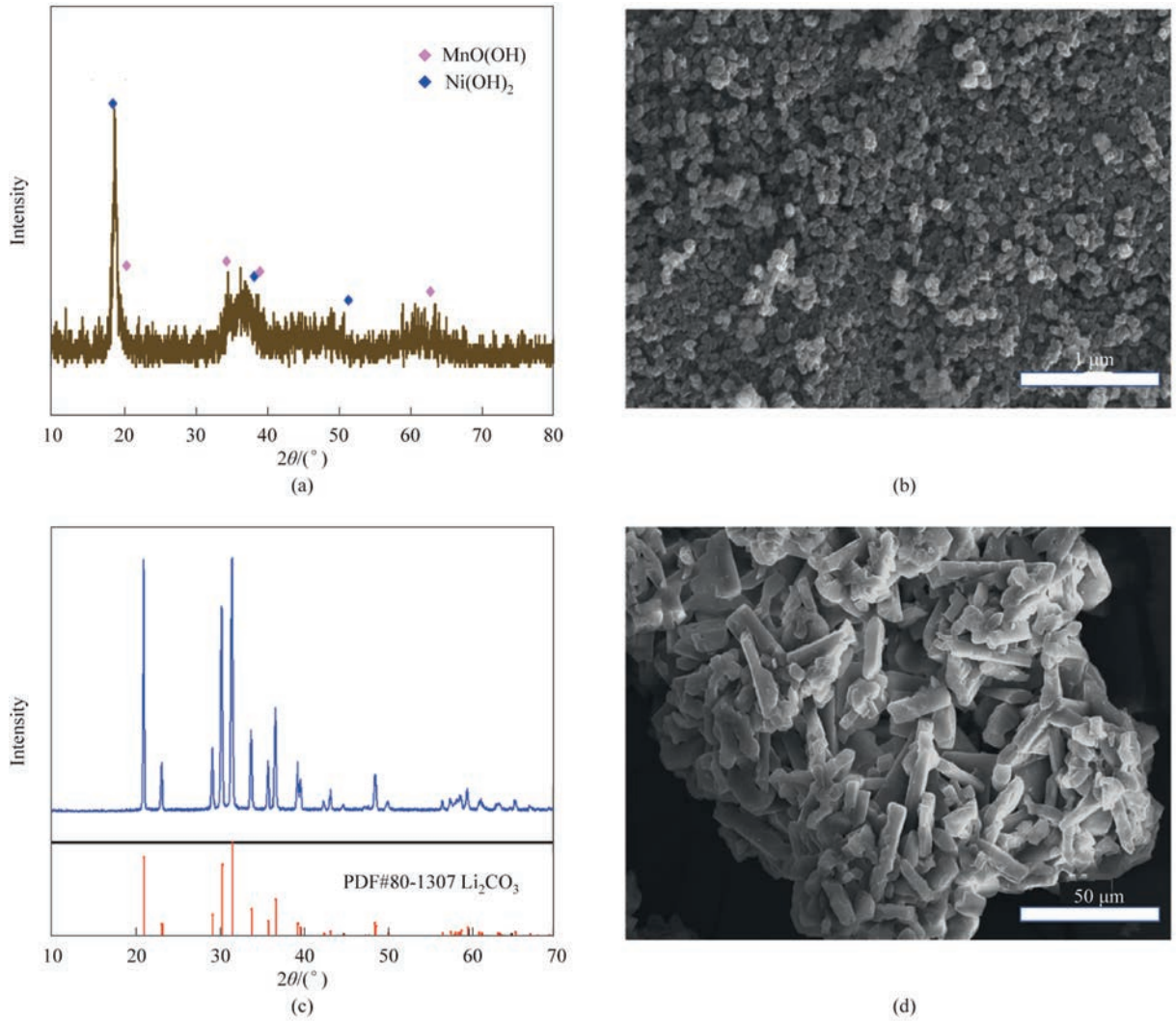

Fig. 10. XRD of Ni, Mn recovered product (a); SEM of Ni, Mn recovered product (b); XRD of recovered Li_2CO_3 (c); SEM of recovered Li_2CO_3 (d).

3.5. Recovery of Li, Ni and Mn

To recovery nickel and manganese from the leach solution, based on the initial concentration of nickel and manganese in the leach solution, pH was calculated for the precipitation of nickel and manganese based on the relationship between the solubility product constant (K_{sp}) and pH of $M(OH)_n$. The initial concentration of precipitation was set to be C_1(M), and the concentration at the time of complete precipitation was set to be $C_{min}(M) = 10^{-5}$ mol·L^{-1}. Therefore, according to Eqs. (4)–(6), the starting precipitation $pH_{start}(M)$ and the complete precipitation $pH_{end}(M)$ could be obtained.

$$K_{sp} = [M^{n+}][OH^-]^n \quad (4)$$

$$K_w = [H^+][OH^-] = 10^{-14} \quad (5)$$

$$pH = -\lg[H^+] \quad (6)$$

When the pH is less than 11, all the nickel and manganese could be precipitated, therefore, adding NaOH solution and controlling the pH to 11, the precipitation of $Ni(OH)_2$ and $Mn(OH)_2$ were obtained. The XRD figure of the precipitation product was shown in Fig. 10(a), and the precipitates were mainly MnO(OH) and $Ni(OH)_2$, Because $Mn(OH)_2$ was easily oxidized, it was oxidized to MnO(OH) by oxygen during the precipitation process in the air atmosphere. Fig. 10(b) showed the SEM image of the precipitate, it could be seen that its micro-morphology was many fine round-like particles.

After precipitation of nickel and manganese, the leaching solution was evaporated to concentrate the concentration of enriched lithium ions, and then at 90 °C, adding the same stoichiometric amount of sodium carbonate to treat the enriched lithium solution, then precipitated lithium in the form of lithium carbonate, thus achieving valuable metal recovery of lithium. Because the solubility of Li_2CO_3 in aqueous solution was inversely proportional to temperature [29], so the precipitated Li_2CO_3 was washed using boiling deionized water to remove residual sodium. SEM and XRD images of Li_2CO_3 were shown in Fig. 10(c) and (d). It could be seen from the SEM image that the recovered Li_2CO_3 exhibited clusters of flocculent agglomerates with rod-like distribution. The XRD diffraction peaks of the recovered Li_2CO_3 were excellent agreement with the standard spectrum (PDF#80-1307), which indicated the high purity of the recovered Li_2CO_3.

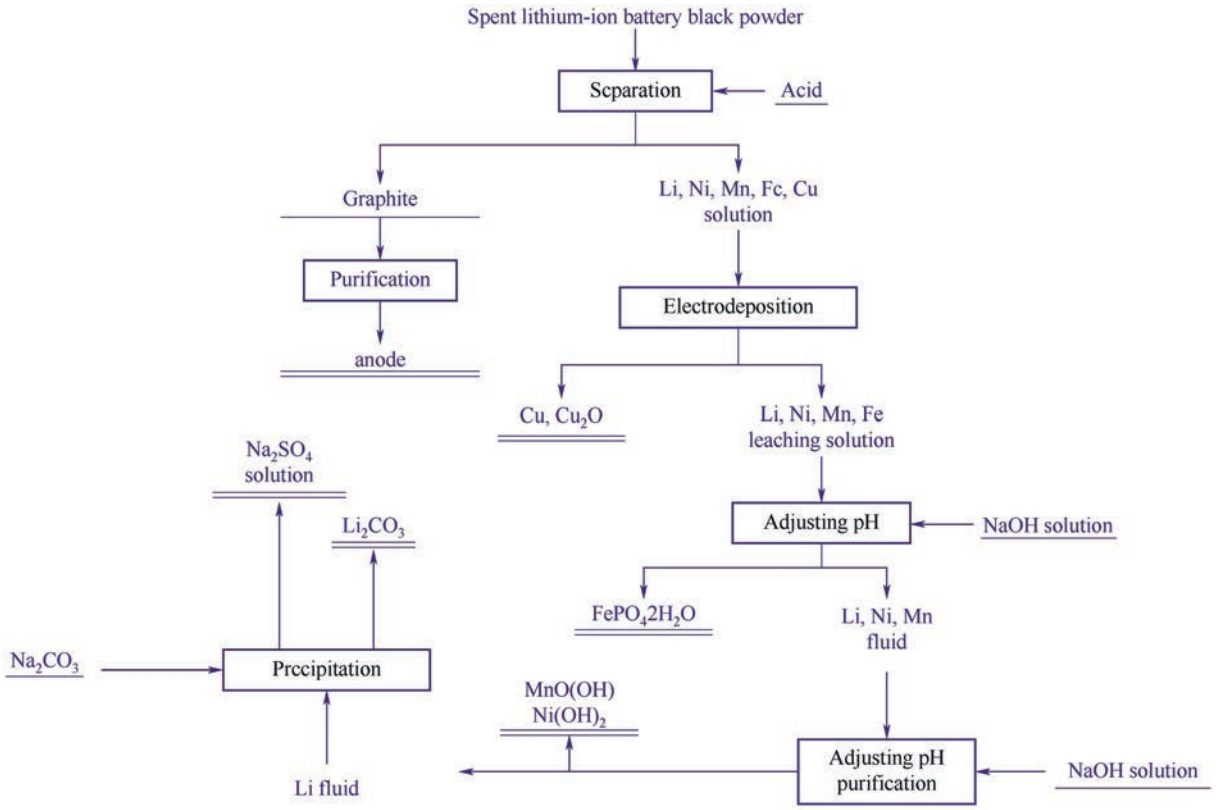

Fig. 11. Recycling flow chart.

3.6. Recovery process of spent lithium-ion battery black mass

In this study, a process for sustainable recovery of black mass was proposed, and the technological flowchart is shown in Fig. 11. The black mass was obtained after spent lithium-ion battery was dismantled and crushed. Sulphur acid solution was used to leach the valuable metals therein, and H_2O_2 was added at the same time in order to leach the metals more efficiently. Manganese, iron, lithium, nickel, aluminum and copper ions were in the leaching solution, and the composition of the leaching residue is graphite. Metallic copper was recovered by electrodeposition, then the pH value was adjusted to 2 to precipitate iron phosphate. The remaining solution was purified by adjusting the pH to remove the small amounts of aluminum and residual iron. Then, a purifying solution containing nickel, manganese and lithium was obtained. The precipitate of manganese hydroxide containing a small amount of nickel by adjusting the pH to 11 with NaOH solution. Lithium carbonate was recovered by adding Na_2CO_3 to the solution, and Na_2SO_4 was recovered by evaporation and crystallization.

4. Conclusions

In this study, an integrated recovery technology of valuable metals from spent lithium-ion battery black mass was developed. A technical route was proposed: acid leaching metals, electrodeposition recovery of copper, recycling of iron phosphate at pH value of 2, removal of aluminum and residual iron at pH value of 7, and precipitation of manganese hydroxide containing a small amount of nickel hydroxide at pH value of 11, and recovery of lithium carbonate by adding Na_2CO_3. The graphite and cathode materials are separated by sulfuric acid solution leaching. Graphite was purified at 600° and then re-prepared into anode material with good electrochemical properties; The copper was well recovered by electrodeposition at the cathode. Good crystalline α-$FePO_4$ was obtained by adjusting the pH to 2, precipitation and roasting. Finally, high purity manganese hydroxide containing nickel was obtained, and lithium is recovered as lithium carbonate.

CRediT Authorship Contribution Statement

Kai Wang: Writing – original draft. Shang Liu: Writing – review & editing, Writing – original draft. Linlin Chen: Writing – review & editing. Yaoguo Huang: Writing – review & editing. Xianfu Sun: Writing – review & editing. Qingyan Chu: Supervision, Writing – review and editing, Validation. Yali Zhang: Supervision, Writing – review & editing, Validation.

Declaration of Competing Interest

The authors declare that they have no known competing financial interests or personal relationships that could have appeared to influence the work reported in this paper.

Acknowledgements

The authors would like to thank the Shandong Provincial Natural Science Foundation, China (ZR2022MB129) for the financial support.

Supplementary Material

Supplementary data to this article can be found online at https://doi.org/10.1016/j.cjche.2025.05.046.

References

[1] Z. Dobó, T. Dinh, T. Kulcsár, A review on recycling of spent lithium-ion batteries, *Energy Rep.* 9 (2023) 6362–6395.

[2] X. Wang, X.M. Zhang, C.M. Zhang, L. Zhang, J.W. Wen, C.X. Wang, G.Y. Huang, Synthesis of high-nickel and high-performance ternary cathode materials through spent lithium-ion batteries recycling system, *Sustain. Chem. Pharm.* 31 (2023) 100959.

[3] N. Cao, Y. Zhang, Z.Q. He, Z.L. Dong, X.Z. Bi, S.S. Kong, L.H. Wang, S.B. He, H. Hu, M.B. Wu, Efficient reduction of spent cathode materials *via in situ* thermal reduction by defect-rich petroleum coke, *Sep. Purif. Technol.* 334 (2024) 126029.

[4] M.Y. Chen, X.T. Ma, B. Chen, R. Arsenault, P. Karlson, N. Simon, Y. Wang, Recycling end-of-life electric vehicle lithium-ion batteries, *Joule* 3 (11) (2019) 2622–2646.

[5] G.X. Ren, C.B. Liao, Z.H. Liu, S.W. Xiao, Lithium and manganese extraction from manganese-rich slag originated from pyrometallurgy of spent lithium-ion battery, *Trans. Nonferrous Metals Soc. China* 32 (8) (2022) 2746–2756.

[6] H. Dang, B.F. Wang, Z.D. Chang, X. Wu, J.G. Feng, H.L. Zhou, W.J. Li, C.Y. Sun, Recycled lithium from simulated pyrometallurgical slag by chlorination roasting, *ACS Sustainable Chem. Eng.* 6 (10) (2018) 13160–13167.

[7] K.H. Gu, X.S. Gao, Y.X. Chen, W.Q. Qin, J.W. Han, Closed-loop recycling of spent lithium-ion batteries based on selective sulfidation: an unconventional approach, *Waste Manag.* 169 (2023) 32–42.

[8] N. Cao, Y.L. Zhang, L.L. Chen, Y. Jia, Y.G. Huang, Priority recovery of lithium and effective leaching of nickel and cobalt from spent lithium-ion battery, *Trans. Nonferrous Metals Soc. China* 32 (5) (2022) 1677–1690.

[9] G.W. Zhang, X. Yuan, C.Y. Tay, Y.Q. He, H.F. Wang, C.L. Duan, Selective recycling of lithium from spent lithium-ion batteries by carbothermal reduction combined with multistage leaching, *Sep. Purif. Technol.* 314 (2023) 123555.

[10] C. Yang, J.L. Zhang, G.Q. Liang, H. Jin, Y.Q. Chen, C.Y. Wang, An advanced strategy of “metallurgy before sorting” for recycling spent entire ternary lithium-ion batteries, *J. Clean. Prod.* 361 (2022) 132268.

[11] F.Y. Su, X.Y. Zhou, X.J. Liu, J. Yang, J.J. Tang, W. Yang, Z.X. Li, H. Wang, Y.Y. Ma, Efficient recovery of valuable metals from spent Lithium-ion batteries by pyrite method with hydrometallurgy process, *Chem. Eng. J.* 455 (2023) 140914.

[12] S.P. Barik, G. Prabaharan, L. Kumar, Leaching and separation of Co and Mn from electrode materials of spent lithium-ion batteries using hydrochloric acid: Laboratory and pilot scale study, *J. Clean. Prod.* 147 (2017) 37–43.

[13] C. Peng, F.P. Liu, Z.L. Wang, B.P. Wilson, M. Lundström, Selective extraction of lithium (Li) and preparation of battery grade lithium carbonate (Li_2CO_3) from spent Li-ion batteries in nitrate system, *J. Power Sources* 415 (2019) 179–188.

[14] P.W. Li, S.H. Luo, L. Zhang, Y.K. Wang, H.R. Zhang, J.H. Wang, S.X. Yan, P.Q. Hou, Q. Wang, Y.H. Zhang, X. Liu, X.F. Lei, W.N. Mu, Study on efficient and synergistic leaching of valuable metals from spent lithium iron phosphate using the phosphoric acid-oxalic acid system, *Sep. Purif. Technol.* 303 (2022) 122247.

[15] X. Xiao, B.W. Hoogendoorn, Y.Q. Ma, S. Ashoka Sahadevan, J.M. Gardner, K. Forsberg, R.T. Olsson, Ultrasound-assisted extraction of metals from Lithium-ion batteries using natural organic acids, *Green Chem.* 23 (21) (2021) 8519–8532.

[16] L. Li, J.B. Dunn, X.X. Zhang, L. Gaines, R.J. Chen, F. Wu, K. Amine, Recovery of metals from spent lithium-ion batteries with organic acids as leaching reagents and environmental assessment, *J. Power Sources* 233 (2013) 180–189.

[17] S.Q. Jiang, X.G. Li, W.T. Zhou, C.Z. Deng, X.N. Zhu, Enhanced green leaching of spent lithium-ion batteries: pyrolysis pretreatment combined with eco-friendly citric acid and ascorbic acid, *Colloids Surf. A Physicochem. Eng. Aspects* 687 (2024) 133492.

[18] G.P. Nayaka, K.V. Pai, G. Santhosh, J. Manjanna, Dissolution of cathode active material of spent Li-ion batteries using tartaric acid and ascorbic acid mixture to recover Co, *Hydrometallurgy* 161 (2016) 54–57.

[19] Y.L. Zhang, W. Chu, X. Chen, M. Wang, H.Y. Cui, J. Wang, Recovery of rare earth metals and synthesis of $Ni_{0.6}Co_{0.2}Mn_{0.2}(OH)_2$ from spent asymmetric-capacitance power batteries, *J. Clean. Prod.* 235 (2019) 1295–1303.

[20] L. Chen, X.C. Tang, Y. Zhang, L.X. Li, Z.W. Zeng, Y. Zhang, Process for the recovery of cobalt oxalate from spent lithium-ion batteries, *Hydrometallurgy* 108 (1–2) (2011) 80–86.

[21] S.X. Yan, Y.D. Ou, X.P. Li, L. Yuan, X.P. Chen, T. Zhou, *In situ* recycling of Al foil and cathode materials from spent lithium-ion batteries through exogenous advanced oxidation, *Sep. Purif. Technol.* 326 (2023) 124788.

[22] W. Chu, Y.L. Zhang, X. Chen, Y.G. Huang, H.Y. Cui, M. Wang, J. Wang, Synthesis of $LiNi_{0.6}Co_{0.2}Mn_{0.2}O_2$ from mixed cathode materials of spent lithium-ion batteries, *J. Power Sources* 449 (2020) 227567.

[23] N. Raje, D.A. Aacherekar, A.V.R. Reddy, Compositional characterization of carbon electrode material: a study using simultaneous TG–DTA–FTIR, *Thermochim. Acta* 496 (1–2) (2009) 143–150.

[24] K. Tatsumi, N. Iwashita, H. Sakaebe, H. Shioyama, S. Higuchi, A. Mabuchi, H. Fujimoto, The influence of the graphitic structure on the electrochemical characteristics for the anode of secondary lithium batteries, *J. Electrochem. Soc.* 142 (3)716–720.

[25] J. Zhang, X.L. Li, D.W. Song, Y.L. Miao, J.S. Song, L.Q. Zhang, Effective regeneration of anode material recycled from scrapped Li-ion batteries, *J. Power Sources* 390 (2018) 38–44.

[26] Y.Q. Li, Y. Zhou, W.L. Ma, P. Wu, X. Cao, X.S. Zhu, S.H. Wei, Y.M. Zhou, Facile fabrication of the hybrid of amorphous $FePO_4 \cdot 2H_2O$ and GO toward high performance sodium-ion batteries, *J. Phys. Chem. Solid.* 176 (2023) 111243.

[27] M. Khachani, A. El Hamidi, M. Kacimi, M. Halim, S. Arsalane, Kinetic approach of multi-step thermal decomposition processes of iron(III) phosphate dihydrate $FePO_4 \cdot 2H_2O$, *Thermochim. Acta* 610 (2015) 29–36.

[28] Y.C. Li, J.H. Hao, F.L. Wei, L. Fu, Y. Liu, Z.J. Wang, C.C. Yang, B.J. Li, Synthesis of Mg-$LiFePO_4$/C composite using intermediate $FePO_4 \cdot 2H_2O$ from $Fe_3(PO4)_2 \cdot 8H_2O$ as precursor *via* an aqueous rheological phase assisted method, *J. Mater. Sci. Mater. Electron.* 27 (9) (2016) 9398–9404.

[29] X.P. Chen, B.L. Fan, L.P. Xu, T. Zhou, J.R. Kong, An atom-economic process for the recovery of high value-added metals from spent lithium-ion batteries, *J. Clean. Prod.* 112 (2016) 3562–3570.